

Article

Characterization of Magnetic and Mineralogical Properties of Slag Particles from WEEE Processing

Asim Siddique^{1,2,*}, Peter Boelens³, Fangchao Long³, Shengqiang Zhou³, Veerle Cnudde^{2,4}
and Thomas Leißner¹

¹ Institute of Mechanical Process Engineering and Mineral Processing, TU Bergakademie Freiberg, 09599 Freiberg, Germany; thomas.leissner@mvtat.tu-freiberg.de

² PProGress-UGCT, Geology Department, Ghent University, B-9000 Ghent, Belgium; veerle.cnudde@ugent.be

³ Helmholtz-Zentrum Dresden-Rossendorf, Institute of Ion Beam Physics and Materials Research, Bautzner Landstrasse 400, 01328 Dresden, Germany; p.boelens@hzdr.de (P.B.); f.long@hzdr.de (F.L.); s.zhou@hzdr.de (S.Z.)

⁴ Environmental Hydrogeology, Department of Earth Sciences, Utrecht University, 3584 CS Utrecht, The Netherlands

* Correspondence: asim.siddique1@mvtat.tu-freiberg.de

Abstract: Magnetic separation has wide-ranging applications in both mineral processing and recycling industries. Nevertheless, its conventional utilization often overlooks the interplay between mineral and particle characteristics and their impact on operational conditions, ultimately influencing the efficacy of the separation process. This work describes a methodology able to achieve the comprehensive characterization and classification of Waste Electrical and Electronic Equipment (WEEE) slag. The primary objective is to establish a meaningful connection between the distinct properties of slag phases and their influence on the separation process. Our methodology consists of several stages. Firstly, the WEEE slag is sieved into distinct size classes, followed by classification into magnetic susceptibility classes by using the Frantz Isodynamic separator. To quantify the magnetic susceptibility of each class, we used a magnetic susceptibility balance, and to identify paramagnetic and ferromagnetic fractions and phases within these magnetic susceptibility classes, we conducted vibrating-sample magnetometer measurements. Finally, to establish a meaningful link between the magnetic characterization, mineralogical, and particle-level details, Mineral Liberation Analysis was conducted for each magnetic susceptibility class. This in-depth analysis, encompassing both particle properties and magnetic susceptibility classes, provides a better understanding of the separation behavior of different phases and can help to enrich phases with a specific range of magnetic susceptibility values. This knowledge advances progress towards the development of predictive separation models that are capable of bridging the gap between theoretical understanding and practical application in the field of magnetic separation.

Keywords: magnetic characterization; magnetic susceptibility classes; WEEE slag; vibrating-sample magnetometer (VSM)



Citation: Siddique, A.; Boelens, P.; Long, F.; Zhou, S.; Cnudde, V.; Leißner, T. Characterization of Magnetic and Mineralogical Properties of Slag Particles from WEEE Processing. *Minerals* **2023**, *13*, 1417. <https://doi.org/10.3390/min13111417>

Academic Editor: Rafael Santos

Received: 10 October 2023

Revised: 24 October 2023

Accepted: 1 November 2023

Published: 7 November 2023



Copyright: © 2023 by the authors. Licensee MDPI, Basel, Switzerland. This article is an open access article distributed under the terms and conditions of the Creative Commons Attribution (CC BY) license (<https://creativecommons.org/licenses/by/4.0/>).

1. Introduction

In the last two decades, advancements in electronic technologies have caused a significant increase in the generation of waste electrical and electronic equipment (WEEE) [1]. This is mostly paired with the increasing number of users, technological advances, and social and economic development [2,3]. The Global E-waste Monitor 2020 reported that in 2019, 53.6 million tons of e-waste was produced, and that this figure is projected to rise to 74 million tons by 2030 [4]; with this expected increase in e-waste, efficient recycling solutions will be even more critical. E-waste has become a major environmental concern, not only because of the pollution it causes, but also due to the loss of valuable and critical elements such as rare earth metals [3,5].

WEEE recycling involves three primary methods: mechanical, hydrometallurgical, and pyrometallurgical. Mechanical recycling aims to recover the metallic and non-metallic components as they are. The effectiveness of physical separation relies on particle characteristics like density, magnetic susceptibility, and size distribution [6]. Hydrometallurgical processing begins with sorting and dismantling, followed by pre-treatment, leaching, purification, and metal recovery [7]. Pyrometallurgical methods rely on thermo-physical metal phase separation behavior, but require high energy. In the case of PCBs, this typically offers sharper and faster separation [8]. Governmental restrictions, statutory recycling rates, and valuable and economically interesting metal contents (e.g., Cu, Au, Ag) have driven technological advancements in the field of pyrometallurgical processing for the recycling of e-waste [3]. However, these industrial processes are designed to recover only major valuable metals from e-waste in the form of a metal phase at the bottom of the furnace. A slag phase forms above the metal phase, containing the ceramic compounds of the feed mix and oxidized metals, as well as some base metal alloys as entrapped droplets. Moreover, these entrapped droplets contain some of the precious metals within the slag [9]. Thus, this slag should be considered as a secondary resource of metals, rather than a waste [10,11]. Such a slag system can have microstructures and mineral phases similar to the primary raw materials. For example, during the cooling process of the slag, various elements can be concentrated in specific crystalline or amorphous phases. These phases can be referred to as “Engineered Artificial Minerals” (EnAM). Treating these slag bodies as ore bodies and applying mineral processing techniques to enrich these EnAMs can help to recover the lost valuable elements in slags.

According to Buchmann et al. (2020), due to the magnetic properties of e-waste slags, magnetic mineral processing operations offer a potential solution able to enrich EnAMs [9]. Similarly, several studies [12–15] have also shown the potential of magnetic separation for slag recycling. Magnetic separation is a high-efficiency, low-cost, and selective technique that relies on the magnetic properties of the minerals present in the slags. The magnetic properties of minerals are determined according to their chemical composition, crystal structure, and electronic configuration [16,17]. Therefore, the magnetic properties of the phases generated in the slag body are highly dependent on their mineralogical and structural composition.

The magnetic separation process relies on the magnetic properties of the particles and the forces acting on them during separation. The magnetic properties of the particles are determined according to several factors, such as their size and composition [18]. The effectiveness of a magnetic separation process depends on the forces acting on the treated particles [19], which, in turn, depend on their corresponding force fields and on various physical particle properties. The magnetic force (F_m ; Equation (1)) acting on the particles is proportional to the applied magnetic flux density (B), the gradient of the flux density (∇B), the mass of a particle (m_p), the difference in the mass magnetic susceptibility of the particle (χ_p) and the medium (χ_f), and inversely proportional to the magnetic permeability of the vacuum (μ_0). The gravitational force (F_g) acting on a particle of density ρ_p , is described by Equation (2), where ρ_f is the density of the medium, V_p is the volume of particle, and g is the gravitational acceleration [18]. These factors can be described using Equations (1) and (2).

$$F_m = \frac{1}{\mu_0} (\chi_p - \chi_f) m_p B \nabla B \quad (1)$$

$$F_g = (\rho_p - \rho_f) V_p g \quad (2)$$

In conventional dry ring-type magnetic separation, for a particle to be recovered in the magnetic concentrate, the magnetic force needs to overcome the gravitational force acting on the particle ($F_m > F_g$). There can be more counteracting forces (F_{coun}) such as drag forces and initial kinetic energy (determined by the flow rate) coming from the media in the case of wet magnetic separation, which need to be overcome by the separating magnetic force ($F_m > F_{\text{coun}}$). If the magnetic force is significantly greater than the counteracting

forces (i.e., $F_m \gg F_{\text{coun}}$), the selectivity of the separation process will be poor, as it fails to differentiate between mineral phases with varying magnetic susceptibility. Similarly, if the valuable phases are in the non-magnetic fraction, the “brute force” approach will result in the poor yield of the non-magnetic fraction, due to the mechanical and magnetic entrainment of the non-magnetic particles in the magnetic tailings. Higher selectivity in the separation process is possible when the magnetic force and counteracting forces have a comparable magnitude ($F_m > F_{\text{coun}}$). Therefore, the selectivity of the process is critically dependent on the relative strengths of the magnetic and counteracting forces acting on the particles. These forces acting on the particles in a specific separator and under certain operating conditions can be estimated by using Equations (1) and (2).

In Equation (1), the magnetic susceptibility of the material (χ_m) is a fundamental property of a particle that describes its response to an applied magnetic field and mathematically can be described as the ratio of the magnetization (M) to the applied magnetic field intensity (H), as shown in Equation (3). However, the magnetic susceptibility of a single particle (χ_p) is the sum of susceptibilities of the individual phases present in the particle, multiplied by their mass fractions (Equation (4)). Therefore, to estimate the magnetic susceptibility of a sample, it is essential that the magnetic susceptibility of the individual phases present in the sample is determined. The magnetic susceptibilities of different phases can vary widely, depending on their composition and structural properties [20].

$$\chi_m = \frac{M}{H} \quad (3)$$

$$\chi_p = \sum_{i=1}^n w_{m,i} \times \chi_{m,i} \quad (4)$$

Several studies [20–24] have shown the importance of determining the magnetic properties of particles to improve and model the efficiency of magnetic separation processes. These studies have also highlighted the complexity of determining the magnetic susceptibilities of particles, which mainly govern the response of a particle to the applied magnetic field. Currently, all our modeling approaches for the magnetic separation process rely mainly on the magnetic susceptibility values obtained from the literature or on establishing elemental proxies to the magnetic susceptibility values, such as the Fe content in the sample material. In a recent study by Guiral-Vega et al. (2022) [21,23], the importance of particle-based characterization for the optimization of magnetic separation processes, based on the magnetic susceptibility classes, is presented. In this study, to create magnetic susceptibility classes, the susceptibility of the phases was assigned by using the average values from the literature, and no characterization methodology for creating magnetic susceptibility classes and determining their magnetic susceptibility values was presented. Moreover, the same mineral phases coming from different ore deposits can have different magnetic susceptibility values due to changes in their crystal structures and slight impurities [17]. Therefore, to optimize and model the magnetic separation process, it is important to first define a methodology for the classification of magnetic susceptibility. Such a dataset with the classified mineralogical, morphological, and physical properties of the particles and phases will greatly contribute to the advanced application of particle-based separation models [20,22,25].

In this study, a methodology able to perform a detailed magnetic characterization of an e-waste slag is presented; this can potentially help to create predictive processing models based on the mineralogical and physical properties of particles. The magnetic properties of the e-waste slag are classified via a pre-treatment with a Frantz isodynamic magnetic separator, followed by direct magnetic susceptibility measurements using the magnetic susceptibility balance (MSB) and magnetic hysteresis loop measurements, obtained using a vibrating-sample magnetometer (VSM). The mineralogical composition and particle properties of the magnetic susceptibility classes are determined using automated mineral liberation analysis (MLA) [26]. Finally, the recoveries of the magnetic phases obtained using the Frantz isodynamic magnetic separator and ring-type magnetic separator are compared

to show the effect of the equipment separation mechanism, which should be considered for predictive processing models. The results of this study provide valuable insights into the magnetic behavior of the different slag phases and physical properties of the particles, and can thus help to develop particle-based separation models.

2. Materials and Methods

The workflow used to create a detailed particle dataset according to the presented characterization methodology is summarized in Figure 1. The methodology consisted of first milling the sample below a 500 μm size fraction, and then classifying the sample material into size classes and subsequently into magnetic susceptibility classes, except <63 μm size classes due to their poor flowability. After size classification, the magnetic susceptibility classes were generated using the Frantz isodynamic separator and their susceptibilities were directly measured with a magnetic susceptibility balance. This method enabled the distribution of phases from each size class based on their susceptibilities into different magnetic susceptibility classes. This, according to Equation (4), reduced the complexity of the phases in each magnetic susceptibility measurement of MSB. For the further characterization of the magnetic susceptibility classes with MLA and VSM, the most suitable size class was selected; more information about this is presented in Section 3.1.

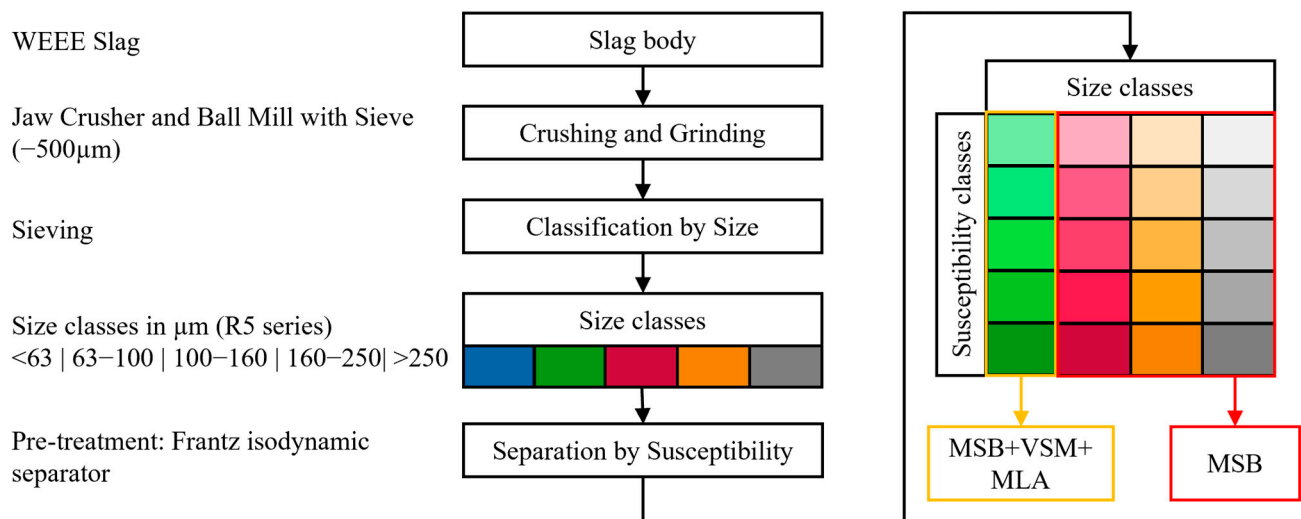


Figure 1. Workflow of the detailed particle characterization, including preparation of the sample material (crushing, grinding) and separation into property classes (size and magnetic susceptibility). Different shades of each color represent different magnetic susceptibility classes. Analysis of the samples was performed using an MSB and a VSM for magnetic properties, as well as MLA for particle properties.

2.1. Sample Material

The sample material used in this study was a slag generated via a melting experiment of finely ground PCB consisting mainly of Cu, Pb, Zn, Al, N, and Sn, which was previously investigated by Buchmann et al. (2020) and Borrowski et al. (2018) [9,27]. The slowly cooling (central) region of the slag body was chosen for this study, due to the relatively large crystal sizes of different phases, making it suitable for magnetic separation processes. The slag body was crushed and milled to <500 μm . The sample material was later sieved into particle size fractions of <63, 63–100, 100–160, 160–250, and >250 μm . To ensure the representativeness of the samples for the characterization and separation experiments, sub-samples were obtained with the help of a riffler and rotary sample splitter.

2.2. Magnetic Classification and Separation

2.2.1. Frantz Isodynamic

A Frantz isodynamic magnetic separator (self-made in former German Democratic Republic) was used to classify the distribution of particle magnetic susceptibility within each particle size fraction [28]. In this separator, particles are separated purely according to their magnetic susceptibility, since the product of the magnetic field strength and field strength gradient is constant at every point in the separation space. Particles for which F_m is large enough to change their trajectory enter the magnetic product. The other less-magnetic particles under the influence of F_g do not change their trajectory and enter the non-magnetic product (Figure 2A). These products (magnetic classes) were generated at an increasing magnetic field strength, as shown in Figure 2B. The increase in the magnetic field strength was achieved by varying the separator current, with values of 0.50 A, 0.70 A, 0.85 A, 1.00 A, 1.15 A, 1.30 A, 1.45 A, and 1.60 A, in an increasing order. The feed material for each magnetic field strength is the insufficiently magnetized fraction of the previous separation round, at a slightly lower field strength. The above-mentioned procedure was used to generate the magnetic classes of the following size fractions: 63–100, 100–160, 160–250, and >250 μm .

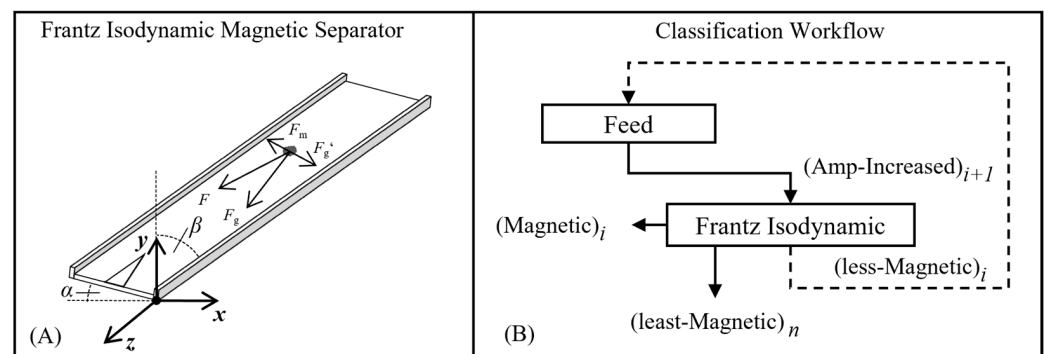


Figure 2. (A) The working principle of the Frantz Iso-dynamic separator and (B) workflow used to create magnetic susceptibility classes using the Frantz isodynamic separator.

The susceptibilities of these magnetic classes can be defined as a range with the help of the calibration curve of the isodynamic separator. These curves can be calculated using Equation (5) for the desired slope angle (β) of the separator, where k is the equipment-specific constant, α is the sideward slope of the separation chute and I is the current (in amperes) supplied to the magnetic coils. In this study, the equipment constant was 70, and the sideward slope angle was kept at 15° for all measurements [20].

$$\chi_m = \frac{k \times \sin \alpha}{I^2} \quad (5)$$

In this study, rather than assuming a range of susceptibilities based on the upper and lower magnetic class prescribed by the Frantz isodynamic magnetic separator, the magnetic susceptibility of each magnetic class was measured directly, using a magnetic susceptibility balance (MSB MK II auto), and the mass-weighted mean magnetic susceptibility of each magnetic class was defined. To minimize the sampling error, three sub-samples were taken from each magnetic fraction, and each sample was measured three times. The mean of all the measurements was used to define the mass-weighted magnetic susceptibility of a single magnetic class.

2.2.2. Ring-Type Magnetic Separator

Magnetic separation experiments of the sample material were performed using a ring-type magnetic separator. This equipment operates as a dry magnetic separator and is based on the lifting principle (Figure 3B). It consists of a conveyor belt (Figure 3-1) on which

the particles are dispersed with the help of a vibrating feeder and are transported through the gap (s) of a magnetic separation system. This gap is formed between two magnetic poles, on the bottom side by the flat ends of a U-shaped pole (Figure 3-2) and on the top side by a rotating ring (Figure 3-3). The working width of the conveyor belt is defined by the width of the flat poles, and the diameter of the rotating ring is larger than the width of the conveyor belt and expands outside of the conveyor on both sides. The particles with $F_m > F_g$ are lifted up and attached to the rotating ring, and are then collected as a magnetic fraction; other particles with a stronger gravitational force remain on the conveyor belt and get collected at the end of the conveyor belt as a less-magnetic fraction. Electromagnetic coils (Figure 3-4) able to generate the desired magnetic field are attached on both sides of the U-shaped core.

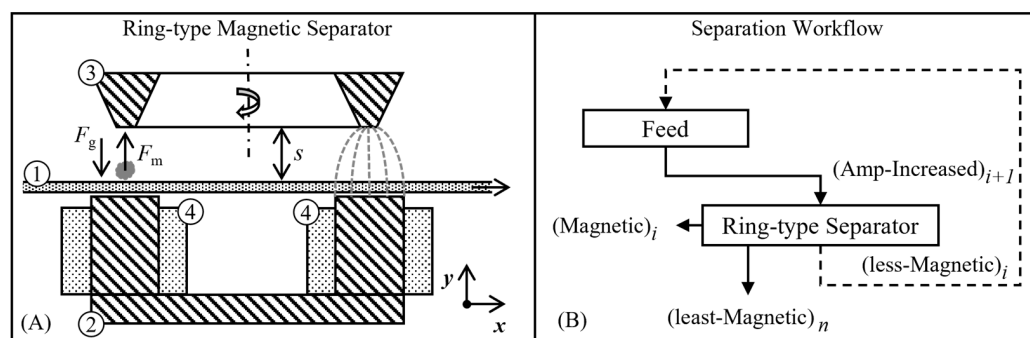


Figure 3. (A) The working principle of the ring-type magnetic separator: 1. Conveyor belt, 2. U-shaped magnet, 3. Rotating ring, 4. Electromagnetic coils. (B) Workflow of the magnetic separation using a ring-type separator.

The particle size fractions of 63–100 μm , 100–160 μm , and 160–250 μm were used for the separation experiments. The magnetic separation was carried out at increasing magnetic field strengths by increasing the separator current, ranging from 0.1 A (minimum) to 1.0 A (maximum) with a step size of 0.1 A. The less-magnetic fraction obtained from the previous separation at a lower magnetic field strength was used as feed material for the next separation, as shown in Figure 3B. The gap between the conveyor belt and the magnetic ring was kept constant at 2 mm throughout all experiments.

2.3. Vibrating Sample Magnetometer (VSM) and Honda-Owens Plot

The magnetic properties of the various classes obtained via the treatment of the 63–100 μm size fraction, with the Frantz isodynamic separator, were thoroughly investigated using measurements obtained with an MPMS3-type SQUID-VSM (Quantum Design GmbH). The M-H curves were measured at 5 K and 300 K. Moreover, the detailed temperature-dependent magnetization was measured at a high field of 4 or 5 T in the range of 5–300 K, as well as with zero-field-cooled (ZFC) and field-cooled (FC) curves at 100 Oe and 500 Oe. For the ZFC/FC measurements, the samples were first cooled down from room temperature to 5 K under zero field. Then, a 100 Oe or 500 Oe was applied, and the ZFC magnetization was measured during warming-up. Subsequently, the FC magnetization was measured during cooling-down under 100 Oe or 500 Oe.

The magnetic behavior of the sample can be determined via the magnetization in function of the magnetic field measurements (M-H curves), and if the sample material consists of paramagnetic or ferromagnetic materials (s.l.), or both of these material types, the magnetic behavior can be identified according to the hysteresis or shape of the M-H curve. If the sample material consists of both paramagnetic and ferromagnetic material (s.l.), then the magnetic susceptibility estimation of the sample can vary depending on the applied magnetic field; this is because the magnetization of ferromagnetic materials is a function of the magnetic field strength and temperature. Therefore, to determine the magnetic susceptibility of the phases, the classes consisting of paramagnetic materials only

should be considered. Using the Honda–Owens plots, it is possible to distinguish the two components of the magnetization from the hysteresis [29–31]. These plots involved plotting the magnetic susceptibility of the sample against the reciprocal of the field strength, in a constant linear region of the magnetization and field. This plot should represent a linear relationship. The slope of this linear relation is equal to the concentration of ferromagnetic material multiplied by the saturation magnetization of the ferromagnetic material (6). The intercept of this slope at the y -axis gives the magnetic susceptibility of the paramagnetic phases [32].

$$\text{Slope} = \text{Conc. Ferromagnetic} \times \text{Saturation Magnetization (ferro)} \quad (6)$$

2.4. Automated Mineralogy Analyses

Automated mineralogy analyses were performed on the MLA system [26,33,34]. The instrument used was an FEI Quanta 650-F field emission SEM (FEI – Thermo Fisher Scientific Inc., Waltham, MA, USA) equipped with two Bruker Quantax X-Flash energy-dispersive X-ray (EDX) detectors (Bruker, Billerica, MA, USA). The MLA Suite software package 3.1.4.686 was used for data processing. The identification of mineral grains using MLA involved segmenting BSE (Back-Scattered Electron) images and collecting the EDX spectra of the particles and grains identified in GXMAP mode, which collects the EDX spectra of each particle in a dense grid and classifies them based on a user-generated list of mineral spectra. All samples were measured using this mode. The measurement conditions of the automated mineralogy and the number of particles analyzed in each sample are summarized in Table 1.

Table 1. Scanning conditions used for MLA measurement and the number of particles analyzed in each measurement.

SEM-EDX Conditions		Sample	Number of Particles
Parameter	Value	63–100 μm	MLA
Mode	GXMAP	Amp 0.50	75,383
Acceleration Voltage	25 kV	Amp 0.70	33,147
Spot Size	5.91 μm	Amp 0.85	61,133
Working Distance	11.99 mm	Amp 1.00	29,782
Beam Current	10 mA	Amp 1.15	65,577
Step Size	10 μm	Amp 1.30	65,869
Brightness	81.7	Amp 1.45	30,392
Contrast	26.6	Amp 1.60	61,484
Spectrum-Matching Threshold	80%	Non-Mag.	68,743

3. Results and Discussion

3.1. Magnetic Susceptibility Classes

The distribution of the magnetic susceptibility classes created using the Frantz isodynamic magnetic separator is shown in Figure 4. The blue lines in Figure 4A are the calibration curves of the Frantz isodynamic separator at 15° [20]. The magnetic susceptibility classes of each size class in Figure 4A are plotted together with the magnetic susceptibility measured using the MSB and the calibration curve of the Frantz isodynamic separator. The magnetic susceptibility classes collected at a lower amperage correspond to higher magnetic susceptibility values, due to the strong magnetic phases in these classes that required lower magnetic field strengths to be recovered in the magnetic fraction. The magnetic susceptibility classes collected at a higher amperage correspond to the lower magnetic susceptibility values, due to the weakly magnetic phases that required higher magnetic field strengths to be recovered in the magnetic fractions.

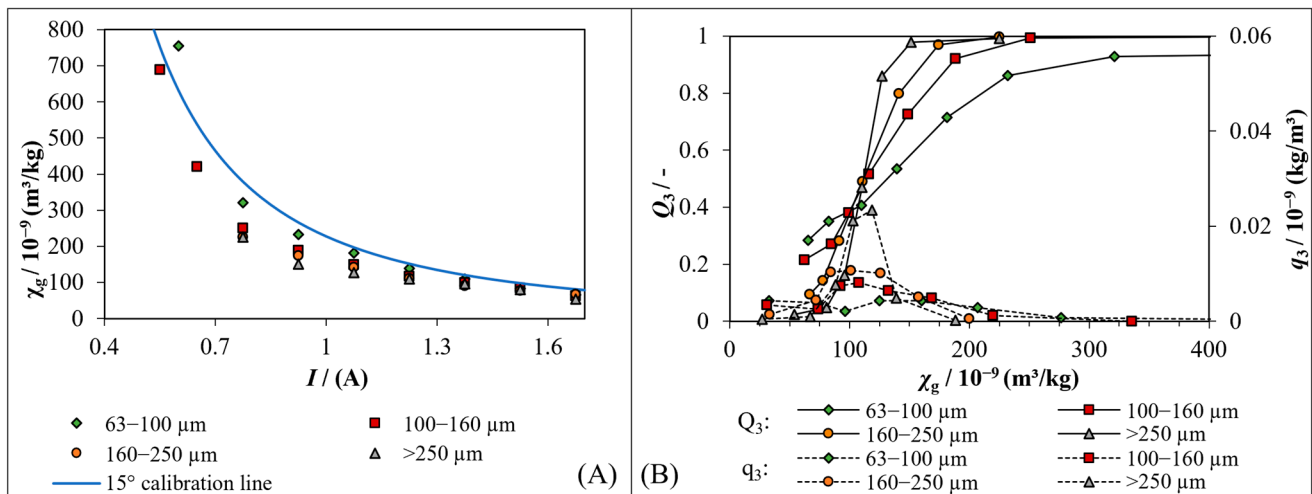


Figure 4. (A) Correlation of current used for separation and measured magnetic susceptibility of different size fractions from WEEE slag. (B) Respective magnetic susceptibility distributions of these size classes obtained according to measurements with a weight balance.

Ideally, the measured susceptibilities would follow the calibration curve, but this is only possible for materials with fixed magnetic susceptibility values or purely paramagnetic phases without any ferromagnetic impurities or magnetic anisotropy [20]. The deviation from the calibration curve observed in Figure 4A is mainly due to the poor liberation of phases in larger particle sizes and the presence of ferromagnetic phases in the WEEE slag. As the particle size reduced (better liberation), the measured magnetic susceptibility values of the magnetic susceptibility classes started to move closer to the actual calibration curves of 15°. While it was possible to obtain a higher number of magnetic susceptibility classes in the range of 50×10^{-9} to $300 \times 10^{-9} \text{ m}^3/\text{kg}$ by applying a wide range of currents, this was not possible for higher magnetic susceptibility ranges due to the narrow possible range of applied currents and the lower mass recoveries of the magnetic fractions, as shown in Figure 4B.

The magnetic susceptibility distribution obtained according to measurements with a weight balance of each size fraction is plotted in Figure 4B, where the slope of the cumulative distribution decreases as the particle size decreases. This trend is also illustrated by the decreasing height of the peak in density distribution (q_3) at the measured magnetic susceptibility (χ_g) range of 75×10^{-9} to $150 \times 10^{-9} \text{ m}^3/\text{kg}$. Decreasing the particle size reduces the complexity of individual particles, as fewer phases are present within each particle (increased liberation). The better the phases are liberated and the fewer composite particles that exist, the more individual peaks in the density distribution will appear.

Having a lower particle size fraction with fewer phases would enable the particle to be recovered in a magnetic susceptibility class that is a better representation of the actual magnetic susceptibility of the phases present in that particle. Therefore, the magnetic susceptibility classes from the finest fraction, i.e., the 63–100 μm size fraction, are used for further mineralogical and magnetic characterization.

3.2. M-H Curves and Honda–Owens Plots

The M-H curves in Figure 5 represent the M as a function of H of the feed material and the magnetic susceptibility classes from the 63–100 μm size fraction. The magnetization response decreases in function of the applied magnetic field strength between the magnetic susceptibility classes collected at 0.5 A to 1.6 A. Due to the distinguishably higher magnetization of the magnetic susceptibility class collected at 0.5 A, it is plotted on the secondary y -axis, and the hysteresis trend of this magnetic susceptibility class demonstrates that the sample mainly consists of ferromagnetic (s.l.) material.

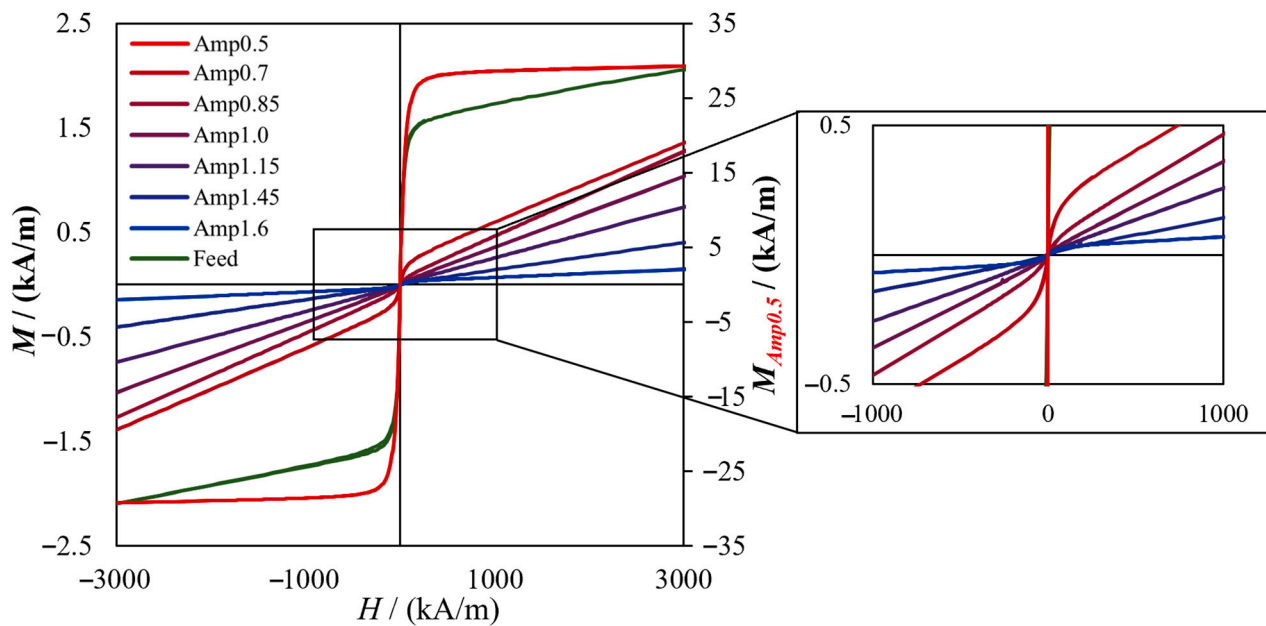


Figure 5. Magnetic hysteresis loop measurements of the magnetic susceptibility classes showing the presence of ferromagnetic phases in the material. Note that the 0.5 A sample shows much higher magnetization and is thus plotted on a secondary axis. The spectrum of colors from red to blue shows the decrease in the magnetization of the magnetic susceptibility classes from Amp 0.5 to Amp1.6.

The M-H curve of the feed sample shows the magnetization response of both ferromagnetic and paramagnetic materials. It shows an initial sharp increase in the magnetization (characteristic of a ferromagnetic material) before starting a linear increase in the magnetization in function of the magnetic field (characteristic of a paramagnetic material). Slightly similar M-H curve trends were also observed for the magnetic susceptibility classes collected at 0.7 A and 0.85 A, but with decreasing ferromagnetic behavior at higher amperages. The rest of the magnetic susceptibility classes showed a hysteresis trend for purely paramagnetic materials.

The major fraction of the ferromagnetic material in the feed was recovered at the lowest applied current (i.e., at 0.5 A). However, the slight ferromagnetic behavior detected in the magnetic susceptibility classes collected at 0.7 and 0.85 A indicates a smaller ferromagnetic inclusion within the particles, along with the major paramagnetic phases. Such magnetic phases can be easily recovered at lower magnetic fields, but their magnetic susceptibility estimation is a challenge; this is because the major part of the magnetic susceptibility measurement can be attributed to the ferromagnetic material. In the case of the magnetic susceptibility classes consisting of ferromagnetic phases, the slope of the magnetization in function of the magnetic field is not constant, and hence the magnetic susceptibility of the sample is field-dependent. Therefore, for the magnetic susceptibility classes in which the magnetic hysteresis loop showed a presence of ferro- and paramagnetic material, “Honda–Owen plots” were used. The concentration of ferromagnetic and paramagnetic phases in the samples, as well as the magnetic susceptibility of paramagnetic phases, can be estimated by using the Honda–Owen plots [31,32].

Along with the feed material, the magnetic susceptibility classes collected at 0.5, 0.7, and 0.85 A displayed ferromagnetic and paramagnetic characteristics in their M-H curve. To further analyze the ferromagnetic and paramagnetic components of these fractions, Honda–Owen plots were created (Figure 6). A linear relationship between the magnetic susceptibility and the reciprocal of the field strength can be observed in these Honda–Owen plots. The slope of this linear relation can be used to estimate the concentration of the ferromagnetic fraction, as described in Equation (6) in Section 2.3, by using the

ferromagnetic saturation magnetization ($M_{\text{ferro.sat}}$) value of $28.0 \text{ kA}\cdot\text{m}^{-1}$, obtained from the M-H curve of the magnetic susceptibility class collected at 0.5 A.

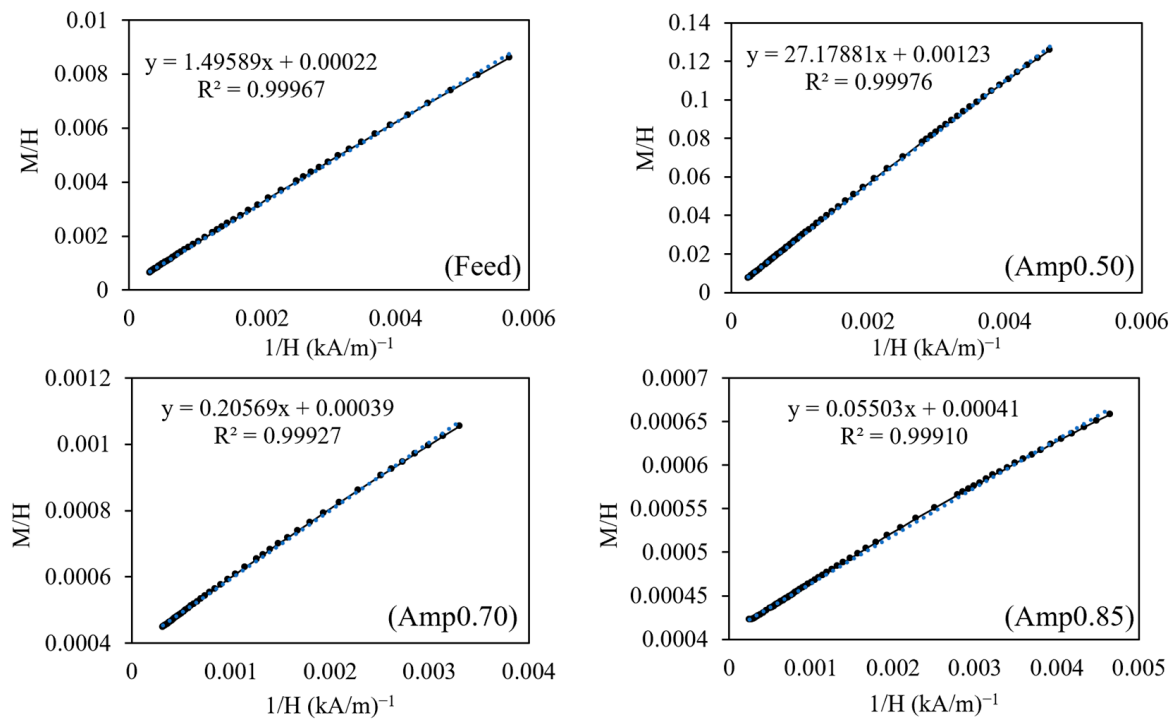


Figure 6. Honda–Owens plots of the magnetic susceptibility classes showing ferromagnetic behavior in their hysteresis measurement. Note the large difference in M/H for the different samples.

The magnetic susceptibility of the paramagnetic phases and relative concentrations of the ferromagnetic and paramagnetic fractions were estimated with the help of Equations (7) and (8), and are given in Table 2. The estimated volume paramagnetic susceptibility (unitless) values obtained using the Honda–Owens method were converted into mass magnetic susceptibility by dividing them according to the sample material’s density. The highest concentration of ferromagnetic material was present in the magnetic susceptibility class collected at 0.5 A; the concentration of the ferromagnetic material decreases as we move to the magnetic susceptibility classes collected at a higher amperage (lower magnetic susceptibility classes).

$$\chi_{\text{para}} = y - \text{axis intercept} \tag{7}$$

$$\text{Slope} = \text{Conc.Ferro}(\%) \times M_{\text{ferro.sat}} \tag{8}$$

Table 2. Estimated concentrations and susceptibilities of the paramagnetic and ferromagnetic material, obtained using the Honda–Owens method.

Sample Name	Conc _{ferro} (%)	Conc _{para} (%)	χ_g (MSB) (m ³ /kg)	$\chi_{g(\text{para})}$ (VSM) (m ³ /kg)	$\chi_{g(\text{ferro})}$ (VSM) (m ³ /kg)
Feed	5.3	94.6	213.6×10^{-9}	146.7×10^{-9}	66.9×10^{-9}
Amp 0.50	97.1	2.9	-	773.2×10^{-9}	-
Amp 0.70	0.7	99.3	755.4×10^{-9}	252.1×10^{-9}	503.3×10^{-9}
Amp 0.85	0.2	99.8	321.0×10^{-9}	234.7×10^{-9}	86.2×10^{-9}

Figure 7 displays the zero-field-cooled (ZFC) and field-cooled (FC) curves acquired at a magnetic field induction of 500 Oe (i.e., 0.05 T). These curves help identify the phases within the ferromagnetic fraction by revealing their magnetic transitions at specific temperatures.

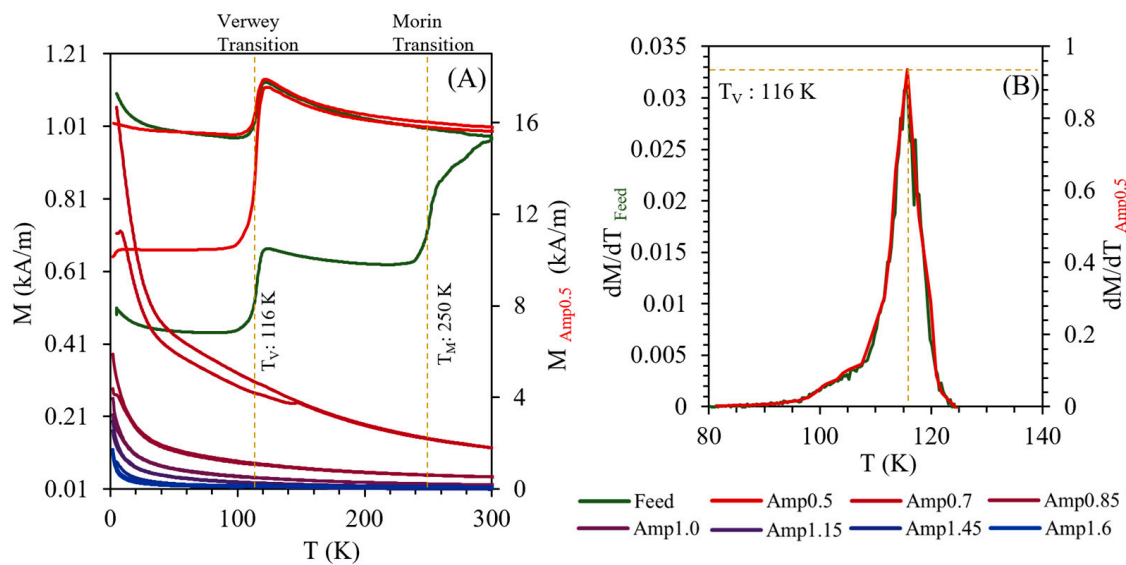


Figure 7. (A) The ZFC–FC curves of the feed and magnetic susceptibility classes with the magnetic transition temperatures, due to the larger magnetization of Amp 0.5, which is plotted on the secondary vertical axis. (B) The derivative of magnetization (M) and temperature (T) representing the Verwey transition temperature of magnetite in the feed (primary vertical axis) and Amp 0.5 (secondary vertical axis).

In Figure 7A, both the feed and Amp 0.5 samples show a noticeable step-like increase in their ZFC and FC curves at 116 K. The jumps observed in both the ZFC and FC curves within the temperature range of 100–120 K correspond to the Verwey transition (T_V) in magnetite [35]. In Figure 7B, the derivative of the magnetization (M) and the temperature (T) from the feed and Amp 0.5 show a peak at 116 K, corresponding to the Verwey transition temperature of magnetite in this study. The Verwey transition represents a low-temperature phase transition in magnetite that induces changes in its magnetic, electrical, and thermal properties [36]. Typically, this transition is expected near 120 K, but can be observed within a range of 80 to 125 K [37]. As the temperature crosses the Verwey transition temperature, the crystal lattice of magnetite transforms, shifting from a monoclinic structure to a metallic cubic inverse spinel structure, which persists at room temperature [38]. Additionally, the ZFC curve of the feed sample displays an additional step increment at 250 K. This particular jump in the ZFC curve of the feed sample at 250 K can be attributed to the Morin transition (T_M), which occurs within the hematite structure [39]. This transition signifies a shift in the spin structure from an antiferromagnetic (at lower temperatures) to a weak ferromagnetic state at room temperature [40]. The small increment in the ZFC curves at low temperatures (around 10 K) shows the traces of nanoparticles [40]. In the ZFC curve of Amp 0.7, a slight jump in the magnetization is visible around 140 K, which could be due to another phase going through the magnetic transition. The ZFC curve at Amp 0.85 did not show a magnetic transition jump; this is due to the low amount of ferromagnetic material in the sample.

3.3. Modal Mineralogy

The phase composition of the magnetic susceptibility classes and the enrichment of specific phases at a certain class can be seen in Figure 8. The order of elements in a phase represents the concentration of an element in that phase; for example, the first element of a phase represents the highest concentration in that phase. The magnetic susceptibility values corresponding to these classes obtained at different amperages can be determined from Figure 4.

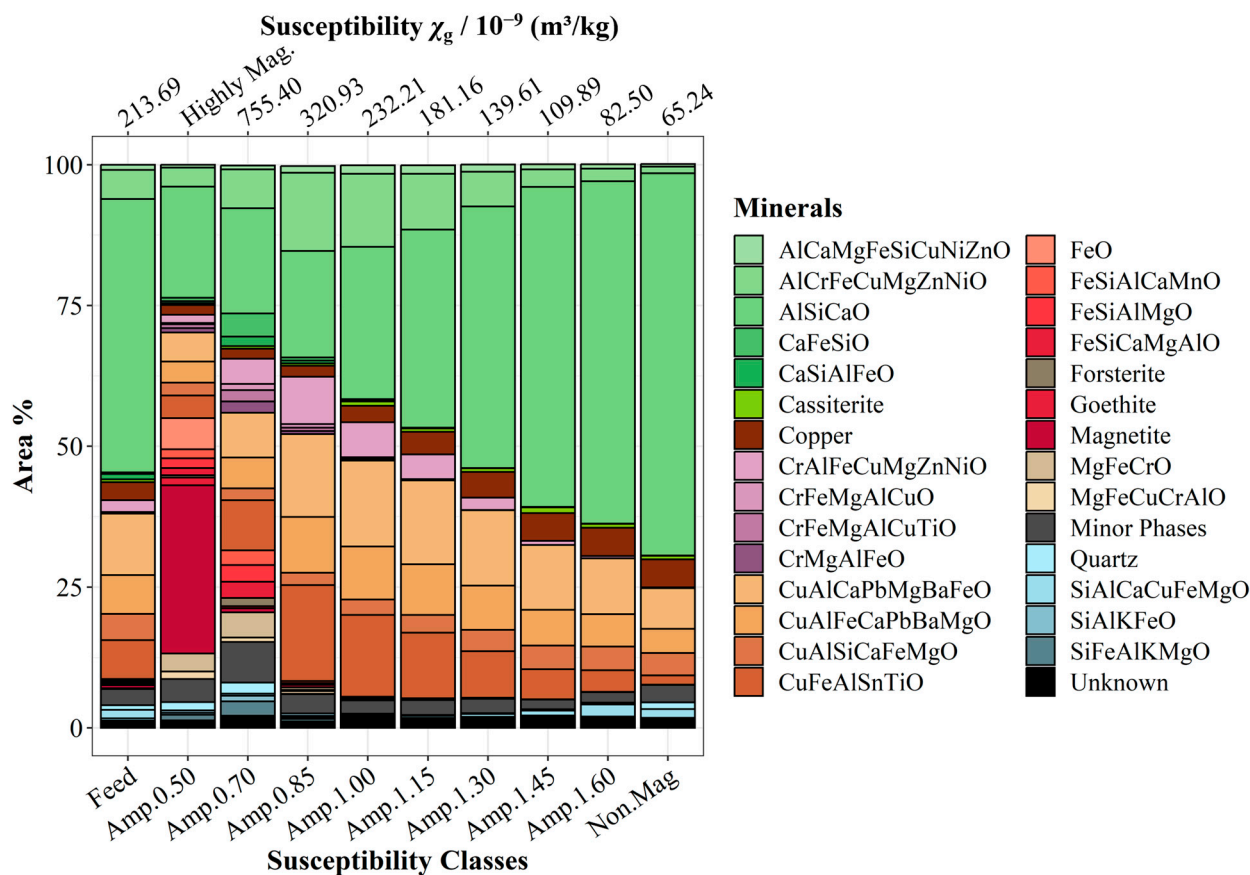


Figure 8. Modal mineralogy of the magnetic susceptibility classes measured using MLA. Different shades of the same color are used to represent the phases with similar compositions.

The Al-rich and Cu-rich phases are the phases that occur most in the magnetic susceptibility classes, except the first one, i.e., Amp 0.5. In the latter, the highest concentration of Fe-rich phases is present and the magnetite phase in this class accounts for 30 area % of the measured particle area in the MLA particle mount. Due to the similar grey-scale and EDX signals from the magnetite and hematite, with MLA, it was not possible to distinguish between them; however, using the ZFC–FC curves, we could identify the presence of weakly ferromagnetic hematite in the feed sample. The concentration of Al-rich phases showed an increasing trend in the lower magnetic susceptibility classes, with the AlSiCaO phase being the highest concentration phase in most of the magnetic susceptibility classes. The Cu-rich phases showed the highest concentration in the Amp 0.85 magnetic susceptibility class, but started to decrease in the lower magnetic susceptibility classes. However, the concentration of pure copper metal increased from higher to lower magnetic susceptibility classes. The Cr-rich phases also showed the highest concentration of 10% at the Amp 0.85 magnetic susceptibility class, and then a decreasing trend towards the lower magnetic susceptibility classes. It can be seen that the different phases accumulate in different classes due to their different magnetic susceptibilities. The broad distribution of the phases across the magnetic susceptibility classes results from strong intergrowth, and thus their association with composite particles.

The distribution of a size fraction into magnetic susceptibility classes helps to break down the complexity of a feed material consisting of particles with a wide range of susceptibilities into smaller ranges of magnetic susceptibility classes. Having more magnetic susceptibility classes could help to reduce the magnetic susceptibility range of particles within each class, but this will be at the expense of the Frantz isodynamic separator requiring a longer separation time. Additionally, even more MLA measurements, as well as magnetic susceptibility measurements with MSB, are thus needed. Therefore, a good bal-

ance between the accuracy of the particle susceptibilities determination and measurement time needs to be considered before coming to a decision regarding the number of magnetic susceptibility classes. In this case study, the number of magnetic susceptibility classes created was adequate to define the magnetic susceptibility of the particles, considering such a complex phase composition. For sample materials with a simpler phase composition, these magnetic susceptibility classes can be even fewer. The enrichment of specific phases within certain magnetic susceptibility classes can help to define the magnetic susceptibility of those phases. For example, the majority of the Cr phases occur in magnetic susceptibility classes collected at Amp 0.70 and Amp 0.85, with a magnetic susceptibility range of 320.90×10^{-9} to $755.40 \times 10^{-9} \text{ m}^3/\text{kg}$. The geometrical properties of the particles occurring in these magnetic susceptibility classes can be obtained using the MLA measurement. However, due to the 2D nature of MLA measurement, these properties will have stereological bias, which can be resolved by using X-ray micro-computed tomography measurements of the particles from each magnetic susceptibility class [41,42].

The elemental content distribution of major elements across paramagnetic susceptibility classes (Amp 0.85—Non. Mag) is represented in Figure 9. From the lower to higher magnetic susceptibility classes, two major trends in the different elemental contents can be observed; the increasing trend is shown by the Fe, Cr, and Mg elements, and the decreasing trend is shown by the Al, Si, and Ca elements. However, the Cu element did not show a consistent trend across all magnetic susceptibility classes.

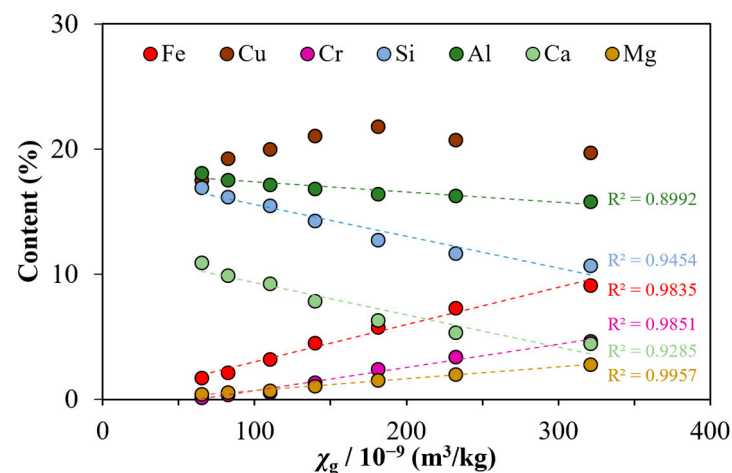


Figure 9. Distribution of selected elements as a function of magnetic susceptibility in particle size fraction of 63–100 μm of WEEE Slag.

The contribution of different elements to different magnetic susceptibility classes can help to define the magnetic susceptibility of the individual particles based on their elemental composition. However, along with the elemental composition of phases, the atomic structural arrangements of phases also play an important role in the overall magnetic susceptibility of a phase, and such effects are prominent in ferromagnetic phases. Nevertheless, considering Fe content as a proxy for the magnetic susceptibility, as performed by [43], can help to define the qualitative magnetization of particles; however, this cannot define the quantitative magnetization of particles unless the contribution of the different Fe contents to the magnetic susceptibility is directly determined, as shown in Figure 9. The increase in magnetic susceptibility has the strongest positive correlation with the Fe content.

3.4. Magnetic Separation

The recovery of magnetic susceptibility classes using the Frantz isodynamic and ring-type separators at different flux densities is presented in Figure 10. The recoveries obtained using the ring-type separator are relatively lower than those obtained using the Frantz isodynamic separator. This discrepancy can be attributed to the distinct particle separation mechanisms employed by each separator.

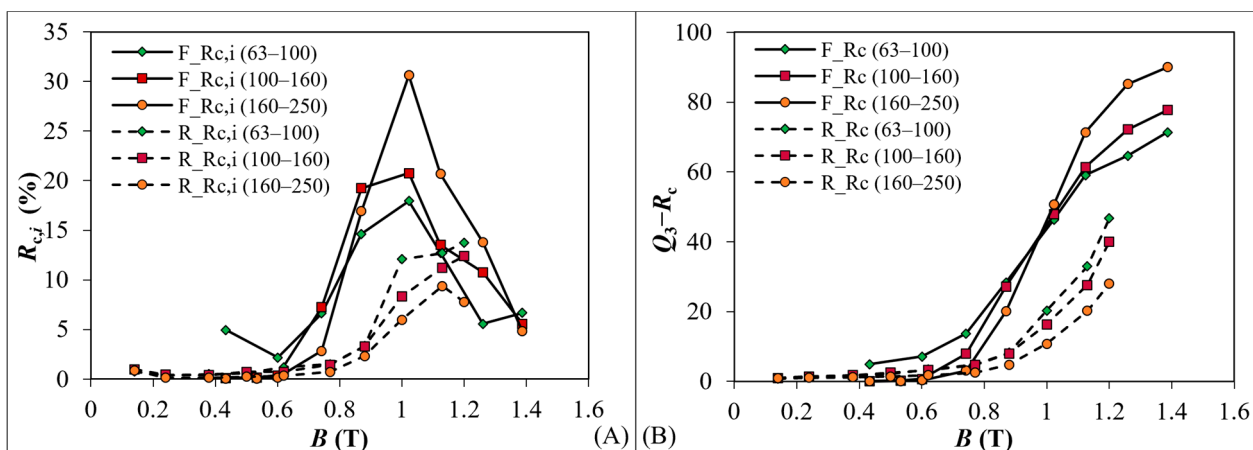


Figure 10. Comparison of the mass recoveries of magnetic phases between Frantz isodynamic separator and ring-type separator over different flux densities. (A) Individual recoveries of each size fraction, and (B) cumulative recoveries of each size fraction.

In the case of the ring-type separator, a particle must possess sufficient magnetic force to be lifted from the conveyor belt and remain attached to the overhead ring to be recovered in the magnetic fraction. Conversely, the Frantz separator operates by attracting particles towards a higher magnetic field gradient, requiring them to flow along this gradient. It is important to note that the Frantz separator is specifically designed for magnetic susceptibility classification and characterization, rather than high-throughput separation. As a result, although the Frantz separator has better recovery rates for magnetic phases compared to the ring-type separator, it takes a longer time to complete the separation process of the same amount of material.

Figure 10 illustrates the recovery of magnetic phases at different particle sizes with a Frantz separator (solid line) and a ring-type separator (dotted line). The individual mass recoveries of the magnetic phases at each size fraction from both separators are shown in Figure 10A. The cumulative mass recoveries are shown in Figure 10B. With the Frantz separator, as the particle size decreases, the recovery of particles also decreases. Conversely, the ring-type separator exhibits the opposite trend, where the recoveries increase as the particle size decreases. This behavior can be attributed to the differing separation mechanisms, as larger particles require a greater magnetic force to be lifted.

4. Conclusions

This publication presents the correlation among magnetic properties and mineralogy, and the particle characteristics of WEEE slag, providing valuable insights into the recovery potential of valuable phases. The key findings and scientific contributions of this study are summarized as follows:

1. Different magnetic susceptibility classes collected at varying amperages exhibited distinct hysteresis trends, indicating the presence of different magnetic phases. Utilizing Honda–Owens plots, the concentrations for ferromagnetic and paramagnetic fractions, as well as the magnetic susceptibility of paramagnetic phases, were estimated. The ZFC–FC curves helped to identify the phases in the ferromagnetic fraction.
2. Modal mineralogy analysis of the magnetic susceptibility classes identified the selective enrichment of the different magnetic phases within the magnetic susceptibility classes. The Al-rich and Cu-rich phases were found to be the most abundant, with the AlSiCaO phase being the dominant phase in most magnetic susceptibility classes.
3. The Cr-rich phases showed the highest recovery in the magnetic susceptibility range of 320.90×10^{-9} to $755.40 \times 10^{-9} \text{ m}^3/\text{kg}$.
4. The elemental distribution analysis revealed distinct trends in major elements across magnetic susceptibility classes. The Fe content showed the strongest positive corre-

lation with magnetic susceptibility, indicating its significant role in magnetization. The Cu element did not exhibit a consistent trend across all magnetic susceptibility classes, due to the poor liberation of Cu-rich phases. The Cr and Mg elements also showed a positive correlation with magnetic susceptibility, which could be due to the Fe–Cr–Mg phases.

5. Magnetic separation experiments using Frantz and ring-type separators demonstrated differences in recovery rates. The Frantz separator exhibited higher recoveries of magnetic phases due to its classification-oriented design, while the ring-type separator showed lower recoveries of magnetic phases due to its high-throughput-oriented design.

Based on the findings, the selective and efficient separation of valuables from slag using magnetic separation needs to overcome the following challenges:

6. Slag has a finely intergrown structure and thus needs fine grinding in order to reduce the number of composite particles. Thus, separation needs to deal with small particles.
7. Slag phases do not have a defined composition, but can vary in their elemental proportions. Thus, their magnetic susceptibility also varies if, for example, the iron content varies.
8. Small inclusions of ferromagnetic phases will have a significant influence on the particle magnetic susceptibility. This may lead to the recovery of non-target particles in a magnetic concentrate.

This detailed mineralogical and magnetic characterization of slags provides a better understanding of the magnetic susceptibility of phases in each magnetic susceptibility class, which makes it possible to define certain magnetic susceptibility ranges in different slag phases. However, further research will be built upon these findings to break down the complexity of magnetic susceptibility classes into susceptibilities of individual phases. This information, combined with the 3D geometrical properties of particles, will be the basis of multi-dimensional separation curves and predictive processing models based on the physical properties of particles.

Author Contributions: Conceptualization, A.S. and T.L.; methodology, A.S. and T.L.; formal analysis, A.S.; investigation, A.S., T.L. and P.B.; resources, T.L., V.C. and S.Z.; data curation, A.S., P.B. and T.L.; writing—original draft preparation, A.S.; writing—review and editing, A.S., T.L., V.C., P.B., F.L. and S.Z.; visualization, A.S.; supervision, T.L. and V.C.; project administration, T.L.; funding acquisition, T.L. All authors have read and agreed to the published version of the manuscript.

Funding: This research was funded by the Deutsche Forschungsgemeinschaft (DFG, German Research Foundation) in the priority program 2315 “Engineered artificial minerals (EnAM)—A geo-metallurgical tool to recycle critical elements from waste streams” with grant number 470202518.

Data Availability Statement: The data presented in this study are available upon request from the corresponding author.

Acknowledgments: The authors acknowledge the support of several staff members of the Institute of Mechanical Process Engineering and Mineral Processing, TU Bergakademie Freiberg, especially Kleen Elvira, for performing sample preparation, separation experiments and magnetic susceptibility measurements (MSB).

Conflicts of Interest: The authors declare no conflict of interest.

References

1. Bhutta, M.K.S.; Omar, A.; Yang, X. Electronic Waste: A Growing Concern in Today’s Environment. *Econ. Res. Int.* **2011**, *2011*, 474230. [CrossRef]
2. Awasthi, A.K.; Cucchiella, F.; D’Adamo, I.; Li, J.; Rosa, P.; Terzi, S.; Wei, G.; Zeng, X. Modelling the correlations of e-waste quantity with economic increase. *Sci. Total Environ.* **2018**, *613–614*, 46–53. [CrossRef] [PubMed]
3. Kumar, A.; Holuszko, M.; Espinosa, D.C.R. E-waste: An overview on generation, collection, legislation and recycling practices. *Resour. Conserv. Recycl.* **2017**, *122*, 32–42. [CrossRef]
4. Forti, V.; Baldé, C.P.; Kuehr, R.; Bel, G. The Global E-Waste Monitor 2020: Quantities, Flows and the Circular Economy Potential. 2020. Available online: https://ewastemonitor.info/wp-content/uploads/2020/11/GEM_2020_def_july1_low.pdf (accessed on 30 March 2023).

5. Robinson, B.H. E-waste: An assessment of global production and environmental impacts. *Sci. Total Environ.* **2009**, *408*, 183–191. [[CrossRef](#)]
6. Cui, J.; Forssberg, E. Mechanical recycling of waste electric and electronic equipment: A review. *J. Hazard. Mater.* **2003**, *99*, 243–263. [[CrossRef](#)]
7. Ashiq, A.; Kulkarni, J.; Vithanage, M. Hydrometallurgical Recovery of Metals From E-waste. In *Electronic Waste Management and Treatment Technology*; Elsevier: Amsterdam, The Netherlands, 2019; pp. 225–246. ISBN 9780128161906.
8. Faraji, F.; Golmohammadzadeh, R.; Pickles, C.A. Potential and current practices of recycling waste printed circuit boards: A review of the recent progress in pyrometallurgy. *J. Environ. Manag.* **2022**, *316*, 115242. [[CrossRef](#)]
9. Buchmann, M.; Borowski, N.; Leifßner, T.; Heinig, T.; Reuter, M.A.; Friedrich, B.; Peuker, U.A. Evaluation of Recyclability of a WEEE Slag by Means of Integrative X-ray Computer Tomography and SEM-Based Image Analysis. *Minerals* **2020**, *10*, 309. [[CrossRef](#)]
10. Shuva, M.; Rhamdhani, M.A.; Brooks, G.A.; Masood, S.; Reuter, M.A. Thermodynamics data of valuable elements relevant to e-waste processing through primary and secondary copper production: A review. *J. Clean. Prod.* **2016**, *131*, 795–809. [[CrossRef](#)]
11. Shen, H.; Forssberg, E. An overview of recovery of metals from slags. *Waste Manag.* **2003**, *23*, 933–949. [[CrossRef](#)]
12. Alanyali, H.; Cöl, M.; Yilmaz, M.; Karagöz, S. Application of magnetic separation to steelmaking slags for reclamation. *Waste Manag.* **2006**, *26*, 1133–1139. [[CrossRef](#)]
13. Lan, Y.; Liu, Q.; Meng, F.; Niu, D.; Zhao, H. Optimization of magnetic separation process for iron recovery from steel slag. *J. Iron Steel Res. Int.* **2017**, *24*, 165–170. [[CrossRef](#)]
14. Ma, Y.; Du, X.; Shen, Y.; Li, G.; Li, M. Crystallization and Beneficiation of Magnetite for Iron Recycling from Nickel Slags by Oxidation-Magnetic Separation. *Metals* **2017**, *7*, 321. [[CrossRef](#)]
15. Menad, N.; Kanari, N.; Save, M. Recovery of high grade iron compounds from LD slag by enhanced magnetic separation techniques. *Int. J. Miner. Process.* **2014**, *126*, 1–9. [[CrossRef](#)]
16. Hunt, C.P.; Moskowitz, B.M.; Banerjee, S.K. Magnetic properties of rocks and minerals. In *Rock Physics & Phase Relations: A Handbook of Physical Constants*; American Geophysical Union: Washington, DC, USA, 1995.
17. Harrison, R.J.; Feinberg, J.M. Mineral Magnetism: Providing New Insights into Geoscience Processes. *Elements* **2009**, *5*, 209–215. [[CrossRef](#)]
18. Svoboda, J. *Magnetic Techniques for the Treatment of Materials*; Kluwer Academic Publishers: Dordrecht, The Netherlands; Boston, MA, USA, 2004; ISBN 1402020384.
19. Oberteuffer, J. Magnetic separation: A review of principles, devices, and applications. *IEEE Trans. Magn.* **1974**, *10*, 223–238. [[CrossRef](#)]
20. Leifßner, T.; Bachmann, K.; Gutzmer, J.; Peuker, U.A. MLA-based partition curves for magnetic separation. *Miner. Eng.* **2016**, *94*, 94–103. [[CrossRef](#)]
21. Guiral-Vega, J.S.; Pérez-Barnuevo, L.; Bouchard, J.; Ure, A.; Poulin, É.; Du Breuil, C. Particle-based characterization and classification to evaluate the behavior of iron ores in drum-type wet low-intensity magnetic separation. *Miner. Eng.* **2022**, *186*, 107755. [[CrossRef](#)]
22. Pereira, L.; Frenzel, M.; Khodadadzadeh, M.; Tolosana-Delgado, R.; Gutzmer, J. A self-adaptive particle-tracking method for minerals processing. *J. Clean. Prod.* **2021**, *279*, 123711. [[CrossRef](#)]
23. Guiral-Vega, J.; Bouchard, J.; Poulin, É.; Ure, A.; Breuil, C.; Pérez-Barnuevo, L. A Phenomenological Model for Particle Kinetics in Drum-type Wet Low-Intensity Magnetic Separation. *IFAC-PapersOnLine* **2022**, *55*, 25–30. [[CrossRef](#)]
24. Boelens, P.; Lei, Z.; Drobot, B.; Rudolph, M.; Li, Z.; Franzreb, M.; Eckert, K.; Lederer, F. High-Gradient Magnetic Separation of Compact Fluorescent Lamp Phosphors: Elucidation of the Removal Dynamics in a Rotary Permanent Magnet Separator. *Minerals* **2021**, *11*, 1116. [[CrossRef](#)]
25. Leifßner, T.; Mütze, T.; Bachmann, K.; Rode, S.; Gutzmer, J.; Peuker, U.A. Evaluation of mineral processing by assessment of liberation and upgrading. *Miner. Eng.* **2013**, *53*, 171–173. [[CrossRef](#)]
26. Fandrich, R.; Gu, Y.; Burrows, D.; Moeller, K. Modern SEM-based mineral liberation analysis. *Int. J. Miner. Process.* **2007**, *84*, 310–320. [[CrossRef](#)]
27. Borowski, N.; Trentmann, A.; Brinkmann, F.; Stürtz, M.; Friedrich, B. Metallurgical Effects of Introducing Powdered WEEE to a Molten Slag Bath. *J. Sustain. Metall.* **2018**, *4*, 233–250. [[CrossRef](#)]
28. McAndrew, J. Calibration of a frantz isodynamic separator and its application to mineral separation. *Proc. Aust. Inst. Min. Metall.* **1957**, *181*, 59–73.
29. Owen, M. Magnetochemische Untersuchungen. Die thermomagnetischen Eigenschaften der Elemente. *Ann. Der Phys.* **1912**, *342*, 657–699. [[CrossRef](#)]
30. Waters, K.E.; Rowson, N.A.; Greenwood, R.W.; Williams, A.J. Characterising the effect of microwave radiation on the magnetic properties of pyrite. *Sep. Purif. Technol.* **2007**, *56*, 9–17. [[CrossRef](#)]
31. Yu, J.; Han, Y.; Li, Y.; Gao, P. Beneficiation of an iron ore fines by magnetization roasting and magnetic separation. *Int. J. Miner. Process.* **2017**, *168*, 102–108. [[CrossRef](#)]
32. Jordens, A.; Sheridan, R.S.; Rowson, N.A.; Waters, K.E. Processing a rare earth mineral deposit using gravity and magnetic separation. *Miner. Eng.* **2014**, *62*, 9–18. [[CrossRef](#)]

33. Schulz, B.; Sandmann, D.; Gilbricht, S. SEM-Based Automated Mineralogy and Its Application in Geo- and Material Sciences. *Minerals* **2020**, *10*, 1004. [[CrossRef](#)]
34. Gu, Y. Automated Scanning Electron Microscope Based Mineral Liberation Analysis an Introduction to JKMRC/FEI Mineral Liberation Analyser. *J. Miner. Mater. Charact. Eng.* **2003**, *2*, 33–41. [[CrossRef](#)]
35. Yang, J.B.; Zhou, X.D.; Yelon, W.B.; James, W.J.; Cai, Q.; Gopalakrishnan, K.V.; Malik, S.K.; Sun, X.C.; Nikles, D.E. Magnetic and structural studies of the Verwey transition in Fe₃–δO₄ nanoparticles. *J. Appl. Phys.* **2004**, *95*, 7540–7542. [[CrossRef](#)]
36. Walz, F. The Verwey transition—A topical review. *J. Phys. Condens. Matter* **2002**, *14*, 285–340. [[CrossRef](#)]
37. Jackson, M.J.; Moskowitz, B. On the distribution of Verwey transition temperatures in natural magnetites. *Geophys. J. Int.* **2020**, *224*, 1314–1325. [[CrossRef](#)]
38. Kostrov, A. Magnetic Properties, Low-Temperature. In *Encyclopedia of Geomagnetism and Paleomagnetism*; Gubbins, D., Herrero-Bervera, E., Eds.; Springer: Dordrecht, The Netherlands, 2007; pp. 515–525. ISBN 978-1-4020-3992-8.
39. Özdemir, Ö.; Dunlop, D.J.; Berquó, T.S. Morin transition in hematite: Size dependence and thermal hysteresis. *Geochem. Geophys. Geosyst.* **2008**, *9*, Q10Z01. [[CrossRef](#)]
40. Cursaru, L.M.; Piticescu, R.M.; Dragut, D.V.; Tudor, I.A.; Kuncser, V.; Iacob, N.; Stoiciu, F. The Influence of Synthesis Parameters on Structural and Magnetic Properties of Iron Oxide Nanomaterials. *Nanomaterials* **2020**, *10*, 85. [[CrossRef](#)]
41. Godinho, J.R.A.; Grilo, B.L.D.; Hellmuth, F.; Siddique, A. Mounted Single Particle Characterization for 3D Mineralogical Analysis—MSPaCMA. *Minerals* **2021**, *11*, 947. [[CrossRef](#)]
42. Siddique, A.; Godinho, J.R.; Sittner, J.; Pereira, L. Overcoming stereological Bias: A workflow for 3D mineral characterization of particles using X-ray micro-computed tomography. *Miner. Eng.* **2023**, *201*, 108200. [[CrossRef](#)]
43. Chehreh Chelgani, S.; Leißner, T.; Rudolph, M.; Peuker, U.A. Study of the relationship between zinnwaldite chemical composition and magnetic susceptibility. *Miner. Eng.* **2015**, *72*, 27–30. [[CrossRef](#)]

Disclaimer/Publisher’s Note: The statements, opinions and data contained in all publications are solely those of the individual author(s) and contributor(s) and not of MDPI and/or the editor(s). MDPI and/or the editor(s) disclaim responsibility for any injury to people or property resulting from any ideas, methods, instructions or products referred to in the content.